JGR Space Physics

RESEARCH ARTICLE
10.1029/2024JA033361

On the Identification of the Dayside Auroral Region Using Incoherent Scatter Radar

Ingeborg Frøystein[1], Andres Spicher[1], Björn Gustavsson[1], Kjellmar Oksavik[2,3], and Magnar Gullikstad Johnsen[4]

[1]Department of Physics and Technology, UiT the Arctic University of Norway, Tromsø, Norway, [2]Department of Physics and Technology, University of Bergen, Bergen, Norway, [3]Department of Arctic Geophysics, The University Centre in Svalbard, Longyearbyen, Norway, [4]Tromsø Geophysical Observatory, UiT the Arctic University of Norway, Tromsø, Norway

Key Points:

- Fast radar scans are used to quantify the relation between electron temperature, density, and heat rate in the dayside F-region ionosphere
- A method combining electron temperature and density is suggested for identification of the winter dayside auroral region
- An electron temperature threshold of 2,000 K (500–1,300 K higher than the background) is used as a proxy for F-region precipitation

Supporting Information:

Supporting Information may be found in the online version of this article.

Correspondence to:

I. Frøystein,
ingeborg.froystein@uit.no

Citation:

Frøystein, I., Spicher, A., Gustavsson, B., Oksavik, K., & Johnsen, M. G. (2024). On the identification of the dayside auroral region using incoherent scatter radar. *Journal of Geophysical Research: Space Physics*, *129*, e2024JA033361. https://doi.org/10.1029/2024JA033361

Received 24 SEP 2024
Accepted 9 DEC 2024

Abstract This paper presents a robust method combining electron temperatures and density to identify the winter dayside auroral region in Incoherent Scatter Radar (ISR) observations. In literature, a common proxy for identifying the dayside auroral region has been enhanced electron temperatures T_e at high altitudes. However, T_e is intimately related to N_e and their relationship is not completely settled. In this study, the relation between T_e, N_e, and the precipitation heat source Q is quantified. Using ESR fast elevation scans in the winter dayside auroral region, the intimate relationship between these three parameters is investigated. T_e decreases roughly linearly with exponentially increasing N_e, irrespective of the heat source. Precipitation creates a heated population with T_e above roughly 2,000 K (i.e., 500–1,300 K higher than the background plasma). Several extensions to the purely T_e based method were examined, and it is found that combining T_e and N_e yields consistent boundaries when compared to magnetic disturbance data from Swarm satellites and 6,300 Å auroral observations. Future applications of characterizing ionospheric dynamics are discussed.

1. Introduction

The high latitude dayside ionsphere is a highly dynamic region which couples to both the thermosphere and magnetosphere, and also the solar wind. In this region particles from several source regions precipitate, manifesting as the dayside aurora and the cusp aurora (Frey et al., 2019). Through the cusp, shocked solar wind (magnetosheath) particles gain direct access to the ionosphere. In addition, particles originating from the open Low Latitude Boundary Layer (open LLBL) and Plasma Mantle, as well as particles from the closed LLBL and Boundary Plasma Sheet (BPS) precipitate in the dayside auroral region (Frey et al., 2019; Newell et al., 2004). Typically, the precipitating energies in the dayside auroral cusp region is lower than in the nightside auroral region, with energies of up to 500 eV (Newell et al., 2006; Vontrat-Reberac et al., 2001), resulting in strong 6,300 Å oxygen emissions at high altitudes (Mende et al., 2016). By extracting the ionospheric regions where we have precipitation, it is possible to study of the effects of solar wind-magnetosphere-ionosphere-thermosphere (SW-M-I-T) coupling in the high latitude dayside ionosphere.

It is a challenging task to identify the dayside auroral region and its boundaries (Lorentzen & Moen, 2000), and they are typically identified differently using various instruments. For optical instruments it is common to consider the ratio of the 6,300 and 5,577 Å emissions (Lorentzen & Moen, 2000), the brightness of the 6,300 Å emission alone (Frey et al., 2019), or the North-South gradient in the 6,300 Å emission (Johnsen et al., 2012). Although optical instruments are invaluable for observing the aurora in high temporal and spatial resolution, they also have limitations caused by clouds, moonlight and season. Single instrument projections of auroral observations are also dependent on an estimated emission height, which can be challenging since the altitude of the 6,300 Å emission can vary significantly (Johnsen et al., 2012; Mende et al., 2016).

Other common methods rely on the in-situ measurements of the flux and energy of the precipitating particles (Newell et al., 2004). The energy and flux criteria developed by Newell et al. (1989) allow to distinguish whether the particles originate from the cusp or a boundary layer. These methods benefit from large data sets and long time series from for example, the Defense Meteorological Satellite Program (DMSP) or National Oceanic and Atmospheric Administration (NOAA) satellites. In general, in-situ observations are limited by the coverage of the satellite trajectory. There is also a significant time separation between individual satellite passes which means that it remains challenging to study the spatio-temporal dynamics of the dayside aurora over a specific region in-situ.

Ground based radars are also commonly used to observe the ionosphere. HF radars such as SuperDARN have been used to identify the cusp region based on observed velocities and spectral intensity and width (e.g., Blanchard et al., 2003; Chisham & Freeman, 2003; Milan et al., 1999). On the other hand, Incoherent Scatter Radar (ISR) can identify the low energy precipitation by observing the enhanced electron temperatures from precipitation-driven heating at high altitudes. Vontrat-Reberac et al. (2001) modeled that a temperature enhancement of 1,000 K is expected due to cusp precipitation. Both Nilsson et al. (1996) and Doe et al. (2001) observed enhanced electron temperatures as a cusp signature, and enhanced temperatures have been used as a signature of low energy precipitation (Kofman & Wickwar, 1984; Vennerstrom et al., 1984; Wickwar & Kofman, 1984). Additionally, McCrea et al. (2000) found that observed auroral emissions matched the enhanced temperatures observed by ISR. The electron temperature has later been used to directly identify the precipitation both on the dayside (Jin et al., 2023; Nishimura et al., 2021) and on the nightside (Aikio et al., 2006; Østgaard et al., 2005). Furthermore, the cusp region has been identified in ISR observations of both N_e and T_e (Nilsson et al., 1996; Nishimura et al., 2021).

However, questions have also been raised about the reliability of electron temperature enhancements as a proxy (Moen et al., 2004). The thermal balance is important, and whether we assume that there is a cusp signature in the electron density or not (Doe et al., 2001; Nilsson et al., 1996), it is crucial to consider the relationship between T_e and N_e to accurately identify the precipitation boundaries. With the possible ambiguities of T_e as an identifier, T_i has also been proposed as a proxy (Lockwood, Davies, et al., 2005; Lockwood, Moen, et al., 2005a, 2005b; Moen et al., 2004). Watermann et al. (1994) observed coincident enhanced T_e, T_i and N_e.

Besides possible direct radar observations of the ionospheric parameters, calculations of the energy loss rate L and energy input or heating rate Q are also essential when investigating the effect of soft electron precipitation into the ionosphere (Kofman & Lilensten, 1992; Kofman & Wickwar, 1984), where large L can be used as a signature of energy input. Estimating Q often relies on modeling, for example, through the electron energy equation (e.g., Abe et al., 1993; Gustavsson et al., 2010; Schunk et al., 1986; Shoucri et al., 1984). As opposed to pure observations-based methods, assessment of Q and L relies on several assumptions and additional atmospheric models for the ionosphere and neutral atmosphere.

Here we present results of quantifying the relationship between T_e, N_e and Q in the dayside auroral precipitation region. We use fast elevation scan data from the European Incoherent Scatter (EISCAT) Svalbard Radar (ESR), providing nearly simultaneous observations of the dayside aurora and the region equatorward of it. This allows to model the effect of N_e on T_e enhancements due to particle precipitation along the vertical column. Based on the ESR scans, we find that an enhancement threshold of 2000 K is appropriate for identifying the dayside auroral precipitation region during boreal winter conditions. Furthermore, using the modeling, we suggest an advanced method based on both T_e and N_e to extract the auroral region based on ISR data. Auroral boundaries obtained from both proposed methods are supported by both optical and in situ observations, and sources of uncertainties in the methods are discussed.

This paper is organized as follows. Section 2 introduces both the data set from the ESR and auxiliary instruments and data. Section 3 presents the modeling results and both methods. It starts with an overview of how the auroral region is identified in the ESR scan data, followed by details of how the relation between T_e, N_e and Q is modeled. Next, the method combining N_e and T_e, as well as a method combining T_e and L is presented. Section 4 presents an event to which the methods are applied and compares the obtained boundary latitudes with auxiliary instruments. Finally, in Section 5, the results are discussed with emphasis on the strength and weaknesses of the method as well as future applications.

2. Instrumentation and Data

This section introduces the instrumentation and data used for this study. The primary data consists of fast geographic North-South (N-S) elevation scans from the ESR at Longyearbyen, Svalbard (78.15° North, 16.03° East). For the elevation scans, the radar was slewing from 30° elevation pointing North to 30° elevation pointing South along the geographic N-S meridian. The experiment mode was 'taro' with a time resolution of 6.4 s. The data were retrieved from the EISCAT Madrigal portal and analyzed with the analysis package GUISDAP (Lihtinen & Huuskonen, 1996). The dates of each experiment and the start and end times are listed in Table 1. For Longyearbyen, the offset from UT to Local Magnetic Time (MLT) is approximately 3 hr, meaning the scans cover approximately 9–14 MLT.

Table 1
Overview of Data Sets Used in This Study

Year	Date	Start time (UT)	End time (UT)	NAL ASI obs.	Swarm pass(es)
2014	20 November	06:30	08:49		
	2 December	06:33	09:58	yes	
	3 December	06:30	08:23	yes	
	4 December	06:30	09:59	yes	
	5 December	06:30	10:29	yes	
	7 December	06:30	07:59		
2015	27 November	06:30	10:58		
	28 November	06:30	10:59		yes
	29 November	09:00	10:59	yes	
	30 November	06:01	10:29	(noisy)	yes
	2 December	06:00	10:29		yes
	5 December	06:00	10:29		yes

Note. The ESR experiment start and end times are listed in columns 2 and 3 for each date. Columns 4 and 5 indicate the availability of optical observations for the NAL ASI or Swarm passes over the ESR, respectively. The NAL ASI data on 30 November 2015 were not used due to noisy data.

Additional data came from optical measurements obtained from the University of Oslo all-sky imager (ASI) in Ny-Ålesund (http://tid.uio.no/plasma/aurora/), and from the Swarm satellites (Friis-Christensen et al., 2008). The Swarm data is retrieved from the Vires Python interface (Smith et al., 2024) with 1 s resolution. Dates where ASI observations or Swarm data are available during the ESR experiment are marked as 'yes' in Table 1. Finally, solar wind data were obtained through the OMNI database (King & Papitashvili, 2005).

Figure 1 summarises the observation platforms for this study. Figure 1a shows the ESR scan footprint at 300 km and the field of view of the ASI in both geographic and Altitude Adjusted Geomagnetic Coordinates (AACGM coordinates) (Burrell et al., 2023; Shepherd, 2014). Figure 1b presents the ESR footprint and three Swarm satellite trajectories on 05 December 2015.

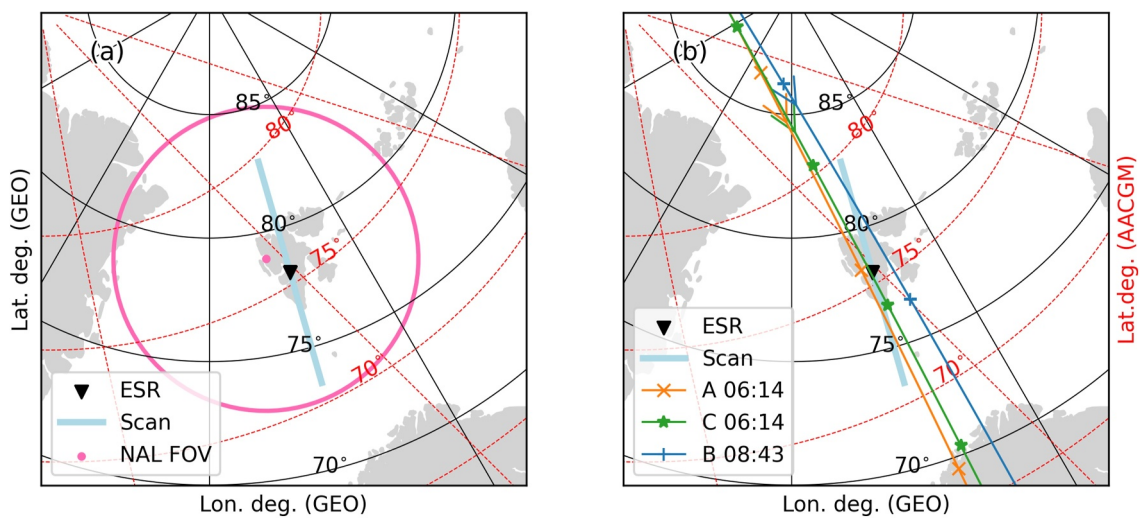

Figure 1. Maps showing the location of the ESR (black triangle) and the ESR low elevation scan footprint at 300 km altitude (light blue). The geographic meridians and latitudes are shown in black, geomagnetic latitude is shown in red. In addition, (a) shows the Ny-Ålesund all-sky camera field of view at 250 km (pink) and (b) Swarm passes from 2015-12-05 (thin solid lines). Swarm spacecraft passes are shown in the legend, where arrows indicate the direction that each spacecraft is heading.

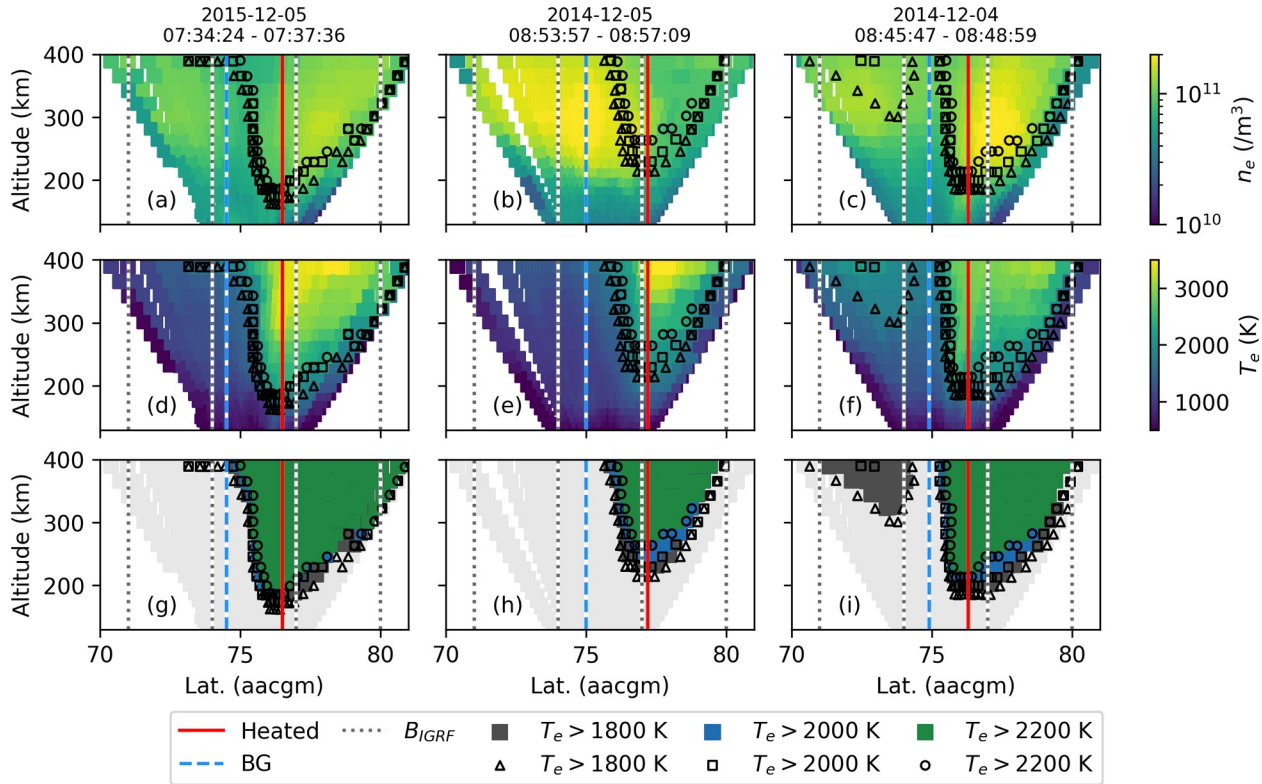

Figure 2. Three individual scans of (a, b, c) N_e (d, e, f) T_e, and (g, h, i) area of enhanced T_e. In the bottom row the three colored regions correspond to threshold values for the enhanced temperature; 1,800 K (gray), 2,000 K (blue), and 2,200 (green). The scattered points in each panel outline the area of enhanced temperatures, where the symbols correspond to the respective threshold values; 1,800 K (triangles), 2,000 K (squares), and 2,200 K (circles). The date and timestamp of each scan is shown on the top of each column. The dashed gray lines show the vertical orientation of the magnetic field (in AACGM coordinates). The solid red and dashed blue lines indicate field-aligned profiles within ('Heated') and southward ('BG') of the identified enhanced T_e area, which are used for the estimation of the relation between T_e and N_e. The scans were filtered with a 2D median filter.

3. Methods for Identification of the Dayside Aurora

Our objective is to provide a simple yet robust method to identify the dayside aurora using ISR measurements which will aid us in characterizing the effects of the SW-M-I coupling in the dayside ionosphere. In this section, we show how the auroral boundaries can be estimated based on only enhanced T_e in ESR fast elevation scans. Then, by modeling electron heating in the dayside ionosphere with ESR observations as input, we investigate in detail the relationship between T_e, N_e and Q. Next, we investigate two possible modifications to the T_e based identification method based on T_e combined with N_e or L. Finally, we discuss possible sources of uncertainty in the auroral boundary latitudes and suggest some quality flags.

3.1. Identification of Enhanced Electron Temperatures in ISR Scan Data

Here, we illustrate how regions of enhanced T_e are identified in ESR N-S scans. A selection of scans are presented in Figure 2, where the top row shows N_e, and the middle row shows T_e. The timestamp and date of each scan are shown above each column. Each scan is filtered with a 2D median filter.

To identify the enhanced T_e in each scan, a T_e threshold value has to be selected. Previous dayside and cusp studies have used thresholds from 1,800 to 3,000 K (Jin et al., 2023; Nilsson et al., 1996; Nishimura et al., 2021). An expected enhancement of 1,000 K above the background ionosphere temperature at 300 km altitude has been found in modeling results (Vontrat-Reberac et al., 2001). Consequently, we use thresholds for T_e of 1,800, 2,000 and 2,200 K in our analysis, which by visual inspection appear to be a good fit for our data set. Our data set consists of only experiments around magnetic noon during the dark winter months around the solar maximum of solar cycle 24. For other magnetic local times, seasons, or years the threshold is likely different.

The bottom row in Figure 2 shows the regions of enhanced T_e above fixed T_e thresholds of 1,800 K (gray), 2,000 K (blue) and 2,200 K (green) which correspond to the regions of precipitation. The outline of the three regions are overlaid on top of all panels in Figure 2 with triangles, squares and circles, respectively. For each threshold value, the equatorward edges of the enhanced T_e region corresponds to the equatorward boundary of the dayside aurora. The boundaries are approximately field-aligned from 250 to 300 km altitude, and the latitude shifts only slightly poleward for increasing T_e enhancement threshold value.

As the background T_e increases with altitude, the choice of threshold value $T_{e,\mathrm{thresh}}$ is also altitude dependent. The value of $T_{e,\mathrm{thresh}}$ =2,000 K is selected for altitudes of 250–300 km, which coincides with the peak altitude for the 630.0 nm emission (Johnsen et al., 2012). In the following, the other two threshold values of 1,800 and 2,200 K, are used as uncertainty estimates for the boundary latitude.

3.2. Evaluating the Effect of N_e on T_e

Irrespective of considering a "cusp signature" in the electron density or not (Doe et al., 2001; Nilsson et al., 1996), variations in the N_e will affect the enhanced T_e value owing to a heat source Q, and the thermal balance is important (e.g., Moen et al., 2004; Wickwar & Kofman, 1984, references therein). For instance, if the same Q is applied, smaller T_e enhancements will be observed for a greater N_e. Consequently, we use modeling to estimate how T_e depends on N_e and Q.

The time and altitude variation of T_e along a magnetic field line is commonly described by the 1D electron energy equation (Abe et al., 1993; Schunk et al., 1986; Shoucri et al., 1984) under the assumption of negligible field aligned plasma drifts (Löfås et al., 2009). This assumption is supported by the fact that we typically do not observe any significant field aligned drift in the experiments used in this study. The resulting 1D energy equation is

$$\frac{3}{2}k_B N_e \frac{\partial T_e}{\partial t} = \frac{\partial}{\partial z}\kappa_e(T_e,z,t)\frac{\partial}{\partial z}T_e + Q_{\mathrm{total}}(z,t) - L(T_e,z,t) \quad (1)$$

where k_B is the Boltzmann constant, κ_e is the electron heat conductivity, Q_{total} is the heat source and L is the heat loss to ions and neutrals (Gustavsson et al., 2010). Following Gustavsson et al. (2010), we estimate Q by solving Equation 1 based on our observed enhanced T_e (heated by precipitation) as well as the observed N_e and T_i. For the ionospheric ion compositions and atmospheric neutral densities the IRI 2016 (Bilitza et al., 2017) and NRLMSIS2.0 (Emmert et al., 2021) models are used, respectively. Both models are evaluated at 78° North, 16° East, where the ESR is located.

The total loss rate L is dependent on T_e, T_i, N_e, and the atmospheric composition as the electrons lose energy to ions and neutrals through collisions and excitation of vibrational and rotational states (Schunk & Nagy, 2009). In addition, excitation of fine structures and the O^1D state are important loss processes to atomic oxygen (Schunk & Nagy, 2009). The cooling is influenced by T_e and the altitude. At 300 km altitude the dominant processes are electron-ion collisions, excitation of fine structure levels in atomic oxygen, and excitation of vibrational states in N_2 (Gustavsson et al., 2010).

The procedure for solving Equation 1 and estimating the relationship between T_e, N_e and Q is described in the following paragraphs. First, for a number of individual scans, regions of enhanced T_e are manually identified and a set of field-aligned strips where T_e is enhanced $\left(T_e^{\mathrm{hot}}\right)$ and T_e is not enhanced $\left(T_e^{\mathrm{cold}}\right)$ are extracted. Such strips are drawn in Figure 2 and plotted as a function of altitude in Figure 3, where blue lines correspond to T_e^{cold} and red lines to T_e^{hot}. This extraction of altitude profiles within and equatorward of the auroral region is key for the procedure and is possible when using fast elevation scan radar observations. Based on the extracted field-aligned strips an estimate of the background heat source Q_{BG} is first calculated before the precipitation heat source Q_{PREC} is calculated.

First, an estimate of the background heat source Q_{BG} which is not caused by precipitation is estimated by solving Equation 1 based on the T_e, T_i, and N_e profiles extracted for T_e^{cold}. For these profiles we assume that there is no significant precipitation since there are no observed T_e enhancements.

The total heat source Q_{total} including both Q_{BG} and heating due to precipitation is estimated by solving Equation 1 based on the T_e, T_i, and N_e profiles extracted for T_e^{hot}. Under the assumption that the background heat source is

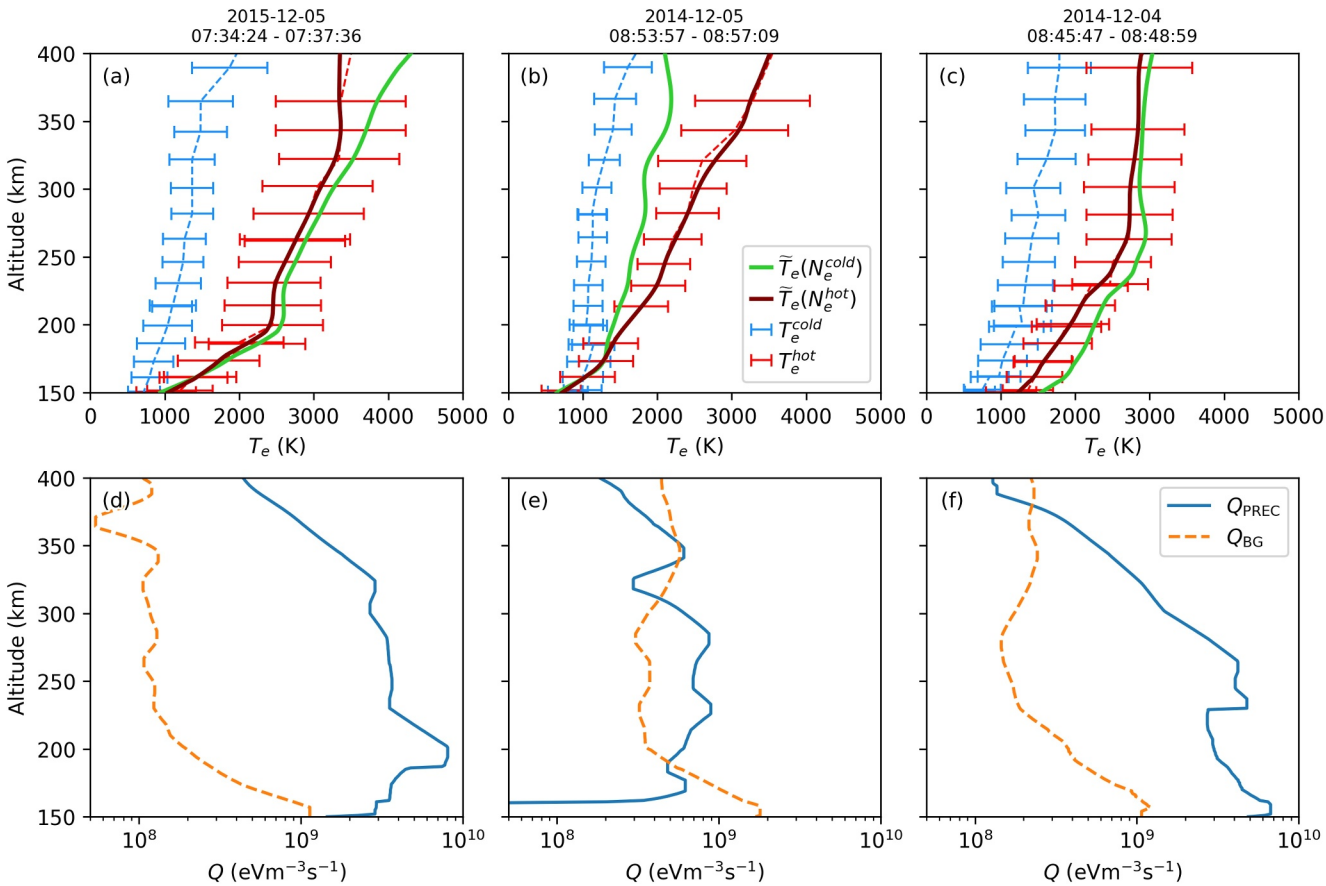

Figure 3. Overview of model altitude profiles of T_e and Q_{PREC}. Panels (a, b, c) show observed T_e (dashed) and modeled $\tilde{T}_e$ (solid) based on open (red) and closed (blue) field lines. Panels (d, e, f) show obtained heat sources Q_{PREC} and Q_{BG}.

uniform with respect to latitude across the entire scan, we estimate the precipitation heat source as $Q_{PREC} = Q_{total} - Q_{BG}$. Heat sources calculated based on the red and blue profiles are plotted as a function of altitude in Figure 3d–3f.

When Q_{PREC} is known, Equation 1 is solved for the model temperature $\tilde{T}_e$ which corresponds to the total temperature including heating due to precipitation. For each scan, the initial electron temperature $T_{e,0}$ is chosen as the $T_e = T_e^{cold}$ profile. This is done under the assumption that in the absence of precipitation, the electron temperature profile is uniform across the scan and corresponding to the background temperature T_{cold}. The lower boundary condition is set to the neutral temperature, and the upper boundary condition is set to T_e^{hot}.

Next, to estimate the relationship between Q_{PREC}, N_e and T_e, the Q_{PREC} and N_e profiles are scaled with scaling factors C_{N_e} and C_Q before solving Equation 1 for the model temperature $\tilde{T}_e$. The set of scaling factors is [0.5, 0.75, 0.9, 1, 1.1, 1.33, 1.66, 2]. For each combination of scaling factors for N_e and Q_{PREC}, the upper boundary condition is scaled by $C_{UB} = \sqrt{C_Q}/C_{N_e}$ to account for the increase and decrease in T_e due to variations in Q_{PREC} and N_e. This scaling is done for each separate scan.

Modeling results of the relationship between T_e, N_e and Q_{PREC} are presented in Figure 3. The top row shows both the observed (dashed) and the modeled (solid) temperatures. The two modeled profiles, $\tilde{T}_e(N_e^{hot})$ and $\tilde{T}_e(N_e^{cold})$ are the solutions to Equation 1 using the N_e and T_i slices corresponding to T_e^{hot} and T_e^{cold}, respectively.

The modeled $\tilde{T}_e$ in the top row of Figure 3 matches well with observed T_e when the obtained Q_{total} is applied to $T_{e,0}$ with N_e^{hot} and T_i^{hot}, as expected. We see larger differences in $\tilde{T}_e$ when Q_{total} is applied to $T_{e,0}$ with N_e^{cold} and T_i^{cold} for the three cases. This is attributed to the difference in N_e on open and closed field lines, shown in Figure 2.

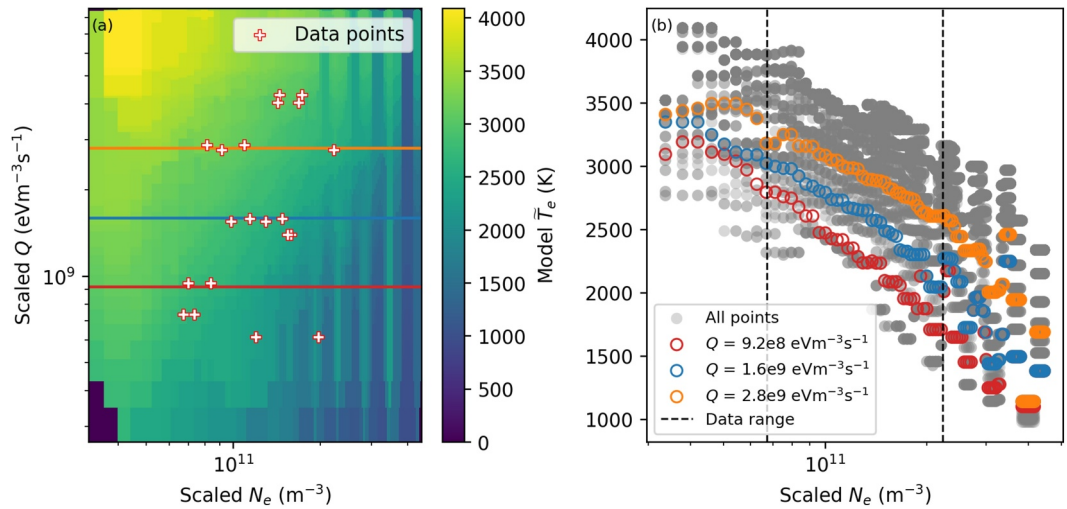

Figure 4. Modeled relationship between T_e, N_e and Q_{PREC} at 300 km. Panel (a) shows $\tilde{T}_e$ (colors) as a function of N_e and Q_{total}. Red and white crosses mark data points. The remaining points are model results when scaling N_e and Q_{PREC}. Panel (b) shows all points of $\tilde{T}_e$ as a function of scaled N_e. The dashed lines indicate the edges of the N_e range in our observed N_e. The red, blue and orange points correspond to $\tilde{T}_e$ for constant values for Q_{total}. The values correspond to the colored lines in panel (a) and are listed in the legend.

For 5 December 2014 (Figure 3b), the electron density is significantly larger on closed field lines, leading to weaker enhancements in $\tilde{T}_e$, which illustrates the strong effect of N_e on T_e.

Panel (a) in Figure 4 shows $\tilde{T}_e$ as a function of N_e and Q_{total}. The data points corresponding to the ESR observations used in the modeling are plotted as red crosses. The remaining points are modeling results when scaling N_e and Q_{PREC} up/down. From this figure, it is obvious that the variation in T_e is strongly affected by both Q_{PREC} and N_e. Indeed, both parameters can introduce changes in T_e of more than 1,000 K in the most extreme cases.

Figure 4b shows all modeled points as a function of only N_e but where points corresponding to three evenly spaced heat source values at 300 km are highlighted. The highlight colors corresponds to the horizontal lines in Figure 4a. The marked slopes in Figure 4b are all approximately linear with exponentially increasing N_e on the data range (dotted black lines) and suggests that the slope itself is not strongly dependent of Q. Nevertheless, the analysis suggests that the slope of T_e with N_e can be useful. This slope will be used as an extension to the purely T_e based identification method.

3.3. Tuning of the T_e Identification Method

As was previously shown, identifying the dayside aurora based solely on T_e is subject to uncertainties due to its intrinsic relation to N_e. Thus, this section presents two methods to account for the N_e effect. Both schemes rely on adjusting the T_e enhancement threshold based on additional parameters, namely L and N_e, as shown in Figure 5 and explained below.

First, an approach based on L is presented. Figure 5a shows the histogram of all pairs L and T_e for the dates in our ESR data set plotted in gray with overlaid red contours. An interesting feature is at $\log_{10}L \approx 10^9$ eV/m^{3}s^{-1} and $T_e \approx 2000$ K where the distribution makes a kink (Figure 5a).

For comparison, the thick cyan contour lines show contour lines of all pairs L and $\tilde{T}_e$ based on the model described in Section 3.2. A remarkable feature is that the model contour generally overlaps with the region above the kink, indicating that the kink reflects a separation between heated and cold background electrons. This is reasonable because both the temperatures and energy losses are larger due to heating, yielding a different relationship between heating and cooling. This indicates that a T_e threshold value of 2,000 K is a good match for this data set.

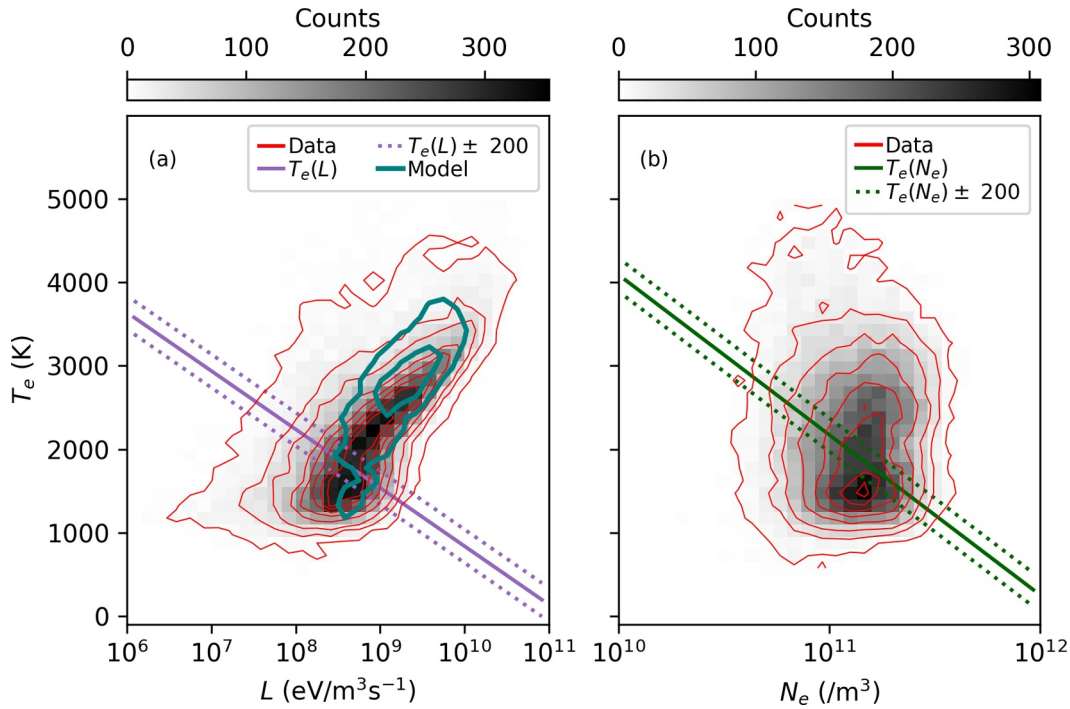

Figure 5. The relationship between loss rate L and T_e. Panel (a) shows a histogram of L and T_e. The red contour lines shows counts of 5, 25, 50, 100, 150, 200, 250 and 290. The purple line shows a separation line which is described in the text. Model contour lines are drawn in blue. Panel (b) shows a histogram of N_e and T_e. The green line show the adaptive threshold $T_e(N_e)$.

Based on the results shown in Figure 5a, a line $T_e(L)$ separating the assumed heated from the cold background distribution is drawn in purple which can be used to identify heated electrons. When this approach is applied, L is first calculated for each point in the ESR data. Next, the threshold $T_e(L)$ is set according to L following the purple line.

Second, a method taking N_e directly into account is presented. Figure 5b shows a histogram and contour lines of all observed N_e and T_e in our ESR data set at 300 km. From this histogram, the average observed N_e for an initial threshold $T_e = 2{,}000$ K, our starting point, is found. The slope obtained from the model in the previous section (shown in Figure 4b) is then placed so that it intersects this point. When the model is applied, $T_e(N_e)$ is adjusted according to the observed N_e in each point. The slope is plotted in solid green in Figure 5b). Dashed green lines show alternative $T_e(N_e)$ lines that are shifted up/down with 200 K.

3.4. Evaluating Uncertainties and Quality Flags

Before applying the method to an example case, suggested quality flags are provided to account for uncertainties in the identified auroral boundaries based on the different methods. The flag criteria are given in Table 2, where the colors 'green', 'yellow' and 'red' refer to increasing uncertainty in the boundary.

Table 2
Value Ranges for Each Quality Flag

Number	Flag proxy	Flag range		
		Green	Yellow	Red
1	T_e uncertainty due to N_e (K)	<300	300 − 500	>500
2	Latitudinal difference (deg.) between different T_e thresholds	<0.8	0.8 − 2	>2
3	Proximity to FOV edge (deg.)	<0.2	0.2 − 0.5	>0.5
4	Number of data gaps (NaNs)	<5	5 − 10	>10

Note. Described in the text.

The first flag is set to account for the uncertainty due to N_e variation. It is found using the N_e along the N-S slice in N_e for each time step. Next, the expected T_e variation due to N_e along the slice is estimated using the model slope shown in Figure 4b. If changes in T_e are greater than 300 K due to N_e, we assume that the boundary latitude is more uncertain. It is important to note that for the method where $T_{e,thresh}$ depend on N_e, this flag is not necessary.

Another possible source of uncertainty is the choice of a temperature enhancement threshold. To account for this, new boundary latitudes are calculated for threshold values $T_{e,thresh} \pm 200$ K. Based on the spread in the differences between the resulting latitudes each point is flagged according to Table 2.

Finally, each point is flagged if it is close to the radar FOV edge or if it is placed in a region where there is a set number of missing data points.

4. Results

In this section, we present one example for which the T_e method and its extensions are applied to identify auroral precipitation regions in ISR scan data. Additionally, comparisons of radar boundaries to established methods based on optical and in-situ observations are presented.

4.1. Method Application to ESR Observations on 5 December 2015

ESR observations and identified auroral regions for an experiment on 5 December 2015 are presented in Figure 6. The first panel shows IMF B_y and B_z components (King & Papitashvili, 2005). The middle five panels show radar 'keograms' of N_e, T_e, T_i, L and $T_{e,\ thresh}(N_e)$. The keograms are made by slicing each scan at a fixed altitude and stacking them in time. This slicing is done from 275 to 325 km altitude before an average is taken. This is done assuming that there is no significant variation in the parameters within this altitude range. Panel g shows the auroral region identified by the $T_e(N_e)$ method. Quality flags colored according to Table 2 are plotted at the top of the panel.

For each panel in Figure 6, curves representing the equatorward boundaries of the precipitation region are overlaid. These are obtained by applying a median filter to the shaded region in Figure 6g and extracting the equatorward edges. The error bars are calculated from the difference between boundaries obtained using $T_{e,thresh} \pm$ 200 K. Panel h in Figure 6 shows the boundaries obtained by all three methods. Their respective enhanced regions, error bars and quality flags are included in Figure S1 in Supporting Information S1. In addition, two additional case examples are included in Figures S2 and S3 in Supporting Information S1.

All three methods seemingly encapsulate the area of enhanced temperatures quite well and there are only slight differences between the obtained latitudes. The error bars obtained with shifting the T_e thresholds by 200 K clearly minimize when the N-S gradient in T_e maximizes. Most of the boundary latitudes are flagged either as green or yellow. The boundary is more certain when the N-S T_e gradient is strong.

As shown in Figure 6a the IMF components are generally stable, with a distinct southward turning $(B_z < 0)$ at approximately 07:30 UT. A northward turning $(B_z > 0)$ follows at approximately 10:00 UT. The N_e is quite smooth until about 09:00 UT, from whereon it is more structured, including possible evidence of patches (Carlson et al., 2006; Lockwood, Davies, et al., 2005; Lockwood, Moen, et al., 2005a; Oksavik et al., 2006). Around this time, B_y appears to be more structured, which is expected to transport structured N_e from the dusk sector into the polar cap (Oksavik et al., 2010). The T_e (Figure 6c) exhibits clear enhancements throughout the experiment, indicating persistent heating due to soft particle precipitation. As IMF turns southward, an equatorward migration and increased T_e can be observed, in line with previous observations (Johnsen & Lorentzen, 2012b; Nishimura et al., 2021). The increase is stronger along the equatorward boundary which is consistent with precipitation on newly opened field lines (Carlson et al., 2004; Lorentzen et al., 2010). In addition, possible poleward moving auroral forms can be seen, typically associated with Flux Transfer Events (FTE) in the dayside magnetopause (e.g., Fasel et al., 1992; McCrea et al., 2000; Milan et al., 1999; Wild et al., 2001). In general, the loss rates L match T_e.

4.2. Comparison With Swarm and ASI Observations

Field-aligned Currents (FACs) are a signature of particle precipitation, and magnetic field perturbation observed by satellite can be used to identify FAC (Lühr et al., 2015). Figure 7a–7c shows perturbations in the magnetic field

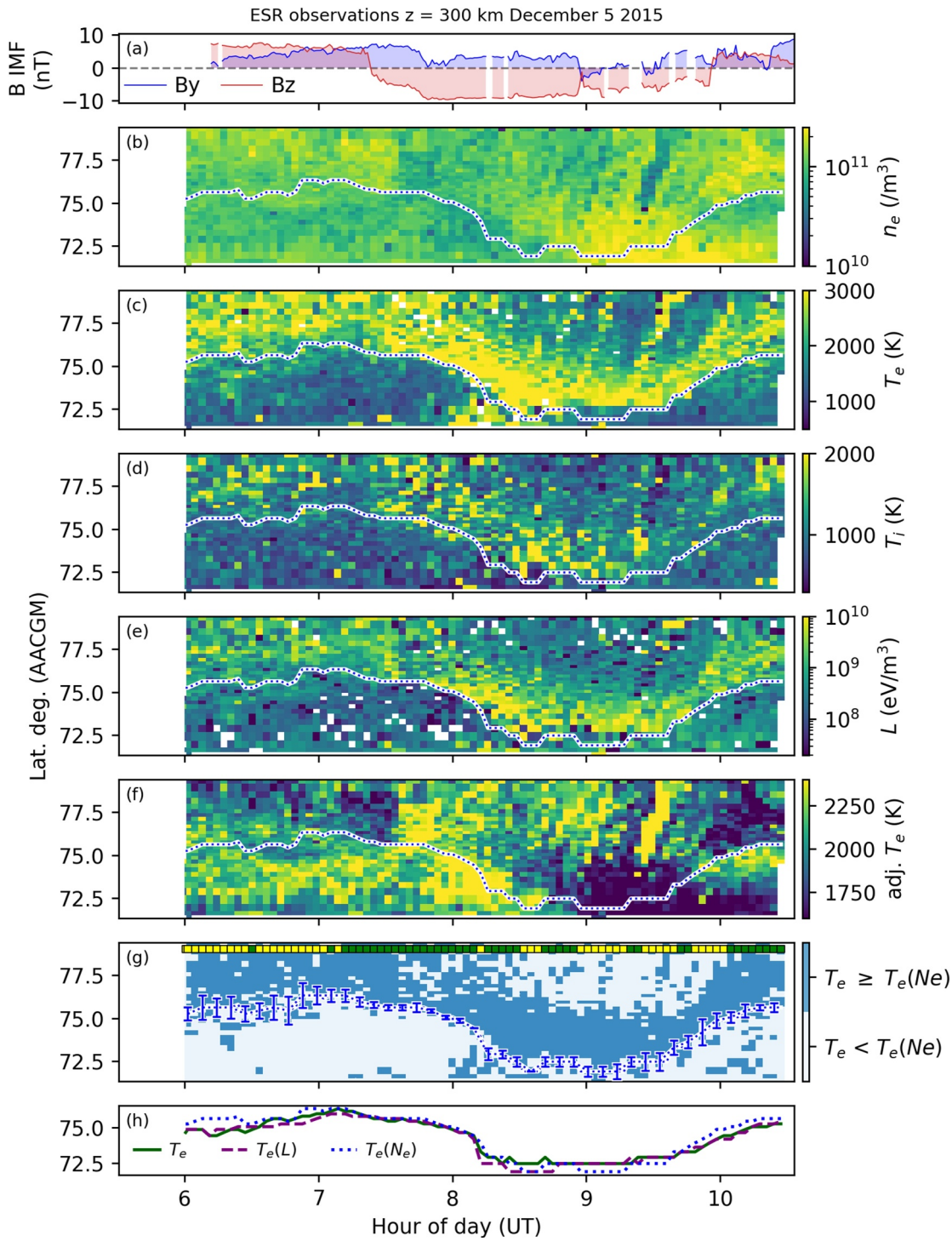

Figure 6. ESR observations and resulting precipitation region boundaries for 2015-12-05. Panel (a) shows the IMF B_y and B_z components, (b) the electron density N_e, (c) the electron temperature T_e, (d) the ion temperature T_i, (e) the electron cooling rates L, (f) the adjusted threshold $T_e(N_e)$, (g) the region of enhanced electron temperatures resulting from the N_e and T_e based method and (h) the three boundaries obtained from all three methods. The quality flags corresponding to Section 3.4 are plotted at the top of panel (g).

Y component (δB_y) observed by Swarm satellites A and C at 06:14 UT and satellite B at 08:43 UT on 5 December 2015 (the same date as the case shown in Figure 6). The perturbations are calculated by subtracting a 25 step Savitzky–Golay filtered component from the original data. For all three passes, the agreements between the

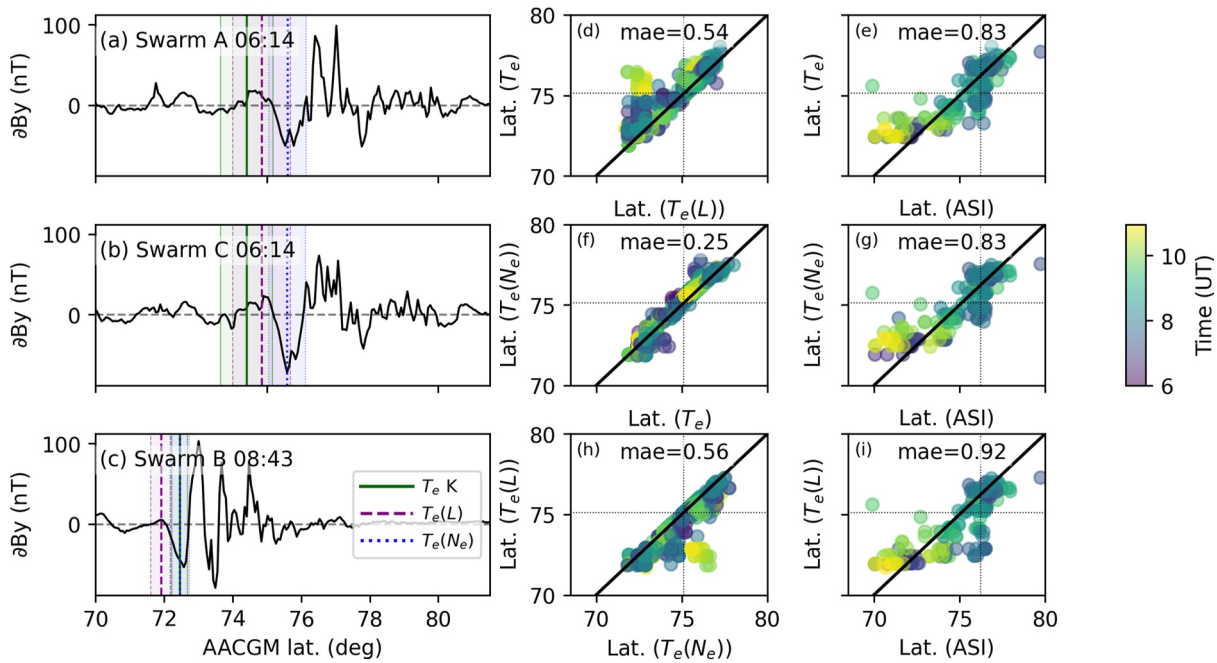

Figure 7. Panels (a, b, c) show perturbations in the magnetic field Y component as observed by Swarm satellites on 5 December 2015. The colored lines correspond to the boundary latitude along the N-S column around the time of the satellite pass. The shading indicates the error bars at the same location. The method is shown in the legend. Panels (d, e, f, g, h, i) show comparisons between boundary latitudes identified by the different radar based method extensions and latitudes identified in 6,300 Å keograms, see the axes labels. Each point is corresponding to the current time (UT). The mean absolute error (mae) is shown in text in each panel. The units on all axes is degrees.

boundaries identified by the radar, shown as vertical lines, and the region of mesoscale field-aligned currents are good, especially at 08:43 UT. The differences are larger at 06:14 UT. In this region the N-S temperature gradient is weaker, and the boundary latitudes obtained by the radar are less certain.

To compare the boundaries obtained by the three radar methods, their latitudes for all experiments listed in Table 1 are plotted in panels dfh in Figure 7. As can be seen, the methods generally agree with a better match between the T_e and $T_e(N_e)$ methods. Only points that are flagged as certain are used in the comparison.

Because enhanced T_e in the high altitude dayside ionosphere is expected to be a proxy for the same low energy precipitation that contributes to the 6,300 Å emission, the radar methods are compared to optical observations. For illustration, two 6,300 Å keograms km from NAL with the dayside precipitation boundary obtained by the $T_e(N_e)$ method overlaid are shown in Figure 8. Plots including the ionospheric parameters and obtained boundaries are included in Figures S2 and S3 in Supporting Information S1. As is seen from the keograms, the ISR auroral boundary for these two events generally encapsulates the dayside aurora.

The ISR boundary latitudes are compared statistically to a previously published method using optical measurements (Johnsen et al., 2012). Here the equatorial boundary of the emission, that is, OCB, is identified as the maximum in the southern gradient of the emission along the magnetic meridian (i.e., from a keogram passing from horizon to horizon through zenith). A pair of empirical formulas are used to map the boundary to an appropriate altitude in order to calculate the corresponding geomagnetic latitude. Following Johnsen and Lorentzen (2012b), erroneous latitudes caused by for example, noisy data are removed. In addition, we remove points where the boundary is placed exactly at the keogram edge, as is done for radar points at the radar FOV edge. The method developed by Johnsen et al. (2012) was by Johnsen and Lorentzen (2012a) successfully tested against particle data from NOAA POES satellites and by Xiong et al. (2014) with FACs determined by CHAMP data. The latter data of the same type as the above mentioned SWARM identified FACs.

The latitudes of the equatorward boundaries obtained from the two instruments are plotted in Figures 7e, 7g and 7i. The radar and ASI latitudes generally show a similar trend. We encounter issues when the boundary latitude is close to the edge of the radar FOV. In the lower left corner, for the lowest latitudes, we clearly see a systematic

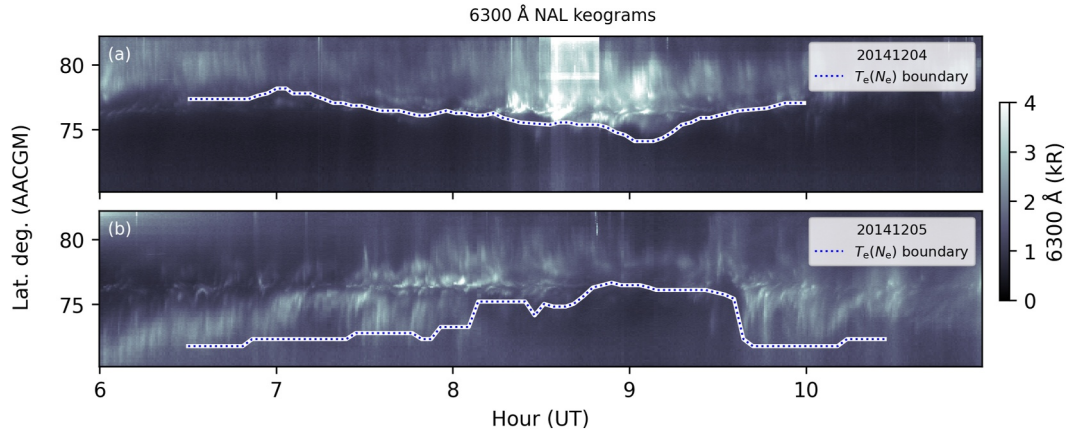

Figure 8. Keograms from the NAL ASI of the 6,300 Å emissions for (a) 4 December 2014 and (b) 5 December 2014. The projection altitude of the emissions is 250 km. The blue dotted lines are the boundaries obtained by the $T_e(N_e)$ method.

error between the ASI and radar latitude. Although there are clearly some differences, the average residual value between the latitudes obtained by ASI and radar is 0.83° for the T_e and $T_e(N_e)$ methods. The residual is slightly larger for the $T_e(L)$ method.

5. Discussion

Identifying the dayside auroral region can be challenging (e.g., Lorentzen & Moen, 2000). For ISR based identification, the relation between N_e and T_e is known to be important (e.g., Moen et al., 2004), and is not fully settled. This raises questions about how to unambiguously identify the regions and various methods and thresholds have been used in literature (Jin et al., 2023; Nishimura et al., 2021). In this study we used ESR fast scans to identify regions of enhanced T_e and modeled the effect of N_e on T_e. We also estimate the heat rate due to precipitation, supplementing previous studies (Abe et al., 1993; Kofman & Wickwar, 1984; Schunk et al., 1986). The ESR data and the model are then used to extend the auroral identification method based only on T_e. Using ESR elevation scans, latitude-altitude ambiguities that are present in constant low-elevation experiments are eliminated.

First, based on modeling of T_e with data extracted from ESR fast scans both within and outside of the precipitation region, we obtain altitude profiles for background and precipitation heat rates separately. When varying Q and N_e we observe that T_e decreases linearly with exponentially increasing N_e at 300 km. A decrease is expected (Moen et al., 2004). In addition, the slopes are similar for all Q calculated.

From both the calculated L for all data points in our ESR data set and the model L, it appears that there are two possible populations in the distribution, shown in Figure 5a). Separating the two populations under the assumption that they describe cool and heated electrons, a separation line can be used to adjust the T_e enhancement threshold in the radar method. This adjustment combines the well-used precipitation proxy T_e with the heat signature L (Kofman & Wickwar, 1984). Coincident regions of high T_e and L were previously observed (Kofman & Wickwar, 1984) and are also clearly visible in the example case in Figure 6. From the distributions of cool and hot electrons T_e enhancements are shown to be typically in the range 600–1,300 K. These values agree with previously modeled T_e enhancements caused by cusp region precipitation (Vontrat-Reberac et al., 2001).

Based on our modeling results of N_e and T_e and the statistical analysis of L we show how a purely T_e identification method can be adjusted by applying adaptive thresholds. These generally agree well, supporting the use of enhanced T_e as proxy. There are, however, some differences in the uncertainties. First, observed N_e depends on calibration via the radar specific system constant. Second, both the Q-T_e-N_e model and the calculation of L depend on atmospheric and ionospheric models such as MSIS (Emmert et al., 2021) and IRI (Bilitza et al., 2017). However, because the obtained model $T_e(N_e)$ slope is independent of the magnitude of Q at the selected altitude and because the slope is adjusted to the average observed N_e this uncertainty is likely not significant in the $T_e(N_e)$ method. Finally, we only use a selected altitude range in all three methods. Therefore, effects of altitude variation in for example, the heat rate Q, which is shown to be variable (Figure 3) are not included.

In general, all three radar methods agree well with each other and with the latitudes obtained using ASI and Swarm FAC. For the comparison with the latitudes obtained with the method by Johnsen et al. (2012), the residuals between the radar and ASI boundary latitudes are less than one degree. A perfect correlation is not expected as the different instruments are subject to a number of uncertainties, not limited to but including, a limited ESR FOV, assumptions of the emission altitude, viewing angle related differences, the influence of partly cloudy skies, thermal emissions (Johnsen et al., 2012; Kwagala et al., 2017) in the ASI observations, and the ESR and ASI not being co-located. For the comparisons, the agreement is often best in the middle between 8 and 9 UT, corresponding to magnetic local noon, when the cusp region precipitation is most likely expected to be above Svalbard (Newell et al., 1989). Here, a stronger N-S T_e gradient is expected (Moen et al., 2004), reducing the uncertainty in the boundary latitudes, as shown in Figure 6.

It is worth noting that the boundary latitudes are not significantly altered when using only T_e or either extension. However, by including N_e it is possible to place the boundary more confidently even in regions of variable N_e. Rather than only flagging and possibly removing points in regions of variable N_e, less data points have to be discarded when using $T_e(N_e)$.

Looking forward, the methods presented can be used to extract altitude profiles of the ionospheric parameters within and outside of the auroral precipitation region. This makes it possible to quantify the statistical response of the ionospheric parameters to changes in the IMF though the SW-M-I coupling. For this use, it is not necessary to discern between the cusp and LLBL/BPS, but to only extract the regions of low energy precipitation. Additionally, for future studies it would be worth investigating whether the expected magnitude of the observed temperature enhancements (Vontrat-Reberac et al., 2001) or possibly observations done at low altitudes could be used to discern between the precipitation source regions.

The method developed in this paper could also be applied to north pointing ISRs located further south, for example, EISCAT VHF legacy data and future EISCAT_3D (McCrea et al., 2015) in order to identify the dayside OCB over Svalbard and from velocity measurements across it, study dayside reconnection rates (Lockwood, Davies, et al., 2005; Lockwood, Moen, et al., 2005a). Furthermore, application of the identified Q/T_e relationships to assess dayside energy flux variations, or even variations in electron number fluxes, may be investigated.

6. Conclusion

An in-depth study was carried out to identify the dayside auroral regions using ESR data during the dark winter time. Fast elevation scans are used to identify regions of enhanced electron temperature T_e where soft precipitation is expected, as well as their cold counterpart on closed field lines within a short time lapse. This allows to model and quantify the relationship between the electron temperature T_e, electron density N_e, and heating rate Q associated with particle precipitation in the dayside F-region ionosphere. The modeling results show that T_e decreases roughly linearly with exponentially increasing N_e, irrespective of the heat source. Furthermore, the data and modeling results of the loss rates L suggest that particle precipitation creates a heated population with T_e roughly above 2,000 K, or enhanced by 600–1,300 K compared to the background plasma.

The analysis on T_e and N_e, and the comparison to optical and in-situ observations, suggests that the $T_e(N_e)$ based method is the preferred method for identification of the dayside auroral region. In general, there are small differences in the boundaries obtained by the three different methods, which supports the robustness of T_e based ISR identification methods. The pure T_e method is simple to implement, but it does not account for variation in T_e due to N_e. The $T_e(L)$ based method is supported by the separation by hot and cold electrons in the data. However, this method relies heavily on the MSIS (Emmert et al., 2021) and IRI (Bilitza et al., 2017) models. The $T_e(N_e)$ method considers the N_e variation but relies on the Q, N_e, T_e model and the radar system constant. Still, to account for uncertainties due to N_e changes, it would be beneficial to adjust the T_e threshold according to N_e.

Using the method(s) it is possible to first obtain the tempo-latitudinal variation of the dayside aurora and its equatorward boundary as well as ionospheric parameters along each vertical column. It allows the characterization of the dynamics of the high latitude, dayside ionosphere due to precipitation caused by the SW-M-I coupling. Such dynamics includes variation in the ionospheric parameters measured directly by the radar, but also Joule heating, density structuring, estimations of the ionospheric conductivities within different regions of the dayside ionosphere with respect to solar wind forcing. It is possible to extend the method to three dimensions with the volumetric capabilities of the upcoming EISCAT_3D (McCrea et al., 2015).

Data Availability Statement

The ESR data is available through the EISCAT Madrigal portal at https://madrigal.eiscat.se/madrigal/. The IMF data were obtained from the GSFC/SPDF OMNIWeb interface at https://omniweb.gsfc.nasa.gov (King & Papitashvili, 2005). The MSIS (Emmert et al., 2021) and IRI (Bilitza et al., 2017) model data were obtained from the Community Coordinated Modeling Center (CCMC) at https://ccmc.gsfc.nasa.gov/models/NRLMSIS~2.0/ and https://ccmc.gsfc.nasa.gov/models/IRI~2016/. The optical observations from the University of Oslo Ny-Ålesund all-sky imager is available at http://tid.uio.no/plasma/aurora/data.php. The Swarm data was downloaded through the VirES Python package available from https://viresclient.readthedocs.io/en/latest/ (Smith et al., 2024). The AACGM conversion Python package is available at https://zenodo.org/records/7621545 (Burrell et al., 2023; Shepherd, 2014).

Acknowledgments
EISCAT is an international association supported by research organisations in China (CRIRP), Finland (SA), Japan (NIPR and ISEE), Norway (NFR), Sweden (VR), and the United Kingdom (UKRI). AS acknowledges the Research Council of Norway (RCN) for the CASCADE project grant (326039). Simulation results of the NRL MSIS and IRI models have been provided by the Community Coordinated Modeling Center (CCMC) at Goddard Space Flight Center through their publicly available simulation services (https://ccmc.gsfc.nasa.gov). The authors thank Lasse Clausen for the UiO Imager data.

References

Abe, T., Oyama, K.-I., Watanabe, S., & Fukunishi, H. (1993). Characteristic features of electron temperature and density variations in field-aligned current regions. *Journal of Geophysical Research (Space Physics)*, *98*(A7), 11257–11266. https://doi.org/10.1029/92JA01970

Aikio, A. T., Pitkänen, T., Kozlovsky, A., & Amm, O. (2006). Method to locate the polar cap boundary in the nightside ionosphere and application to a substorm event. *Annales Geophysicae*, *24*(7), 1905–1917. https://doi.org/10.5194/angeo-24-1905-2006

Bilitza, D., Altadill, D., Truhlik, V., Shubin, V., Galkin, I., Reinisch, B., & Huang, X. (2017). International reference ionosphere 2016: From ionospheric climate to real-time weather predictions. *Space Weather*, *15*(2), 418–429. https://doi.org/10.1002/2016SW001593

Blanchard, G. T., Ellington, C. L., & Baker, K. B. (2003). Comparison of dayside magnetic separatrix signatures in hf and incoherent scatter radar data. *Journal of Geophysical Research*, *108*(A12), 1456. https://doi.org/10.1029/2003JA009910

Burrell, A. G., van der Meeren, C., Laundal, K. M., & van Kemenade, H. (2023). aburrell/aacgmv2: Version 2.6.3. *Zenodo*. https://doi.org/10.5281/zenodo.7621545

Carlson, H. C., Moen, J., Oksavik, K., Nielsen, C. P., McCrea, I. W., Pedersen, T. R., & Gallop, P. (2006). Direct observations of injection events of subauroral plasma into the polar cap. *Geophysics Research Letters*, *33*(5), L05103. https://doi.org/10.1029/2005GL025230

Carlson, H. C., Oksavik, K., Moen, J., & Pedersen, T. (2004). Ionospheric patch formation: Direct measurements of the origin of a polar cap patch. *Geophysics Research Letters*, *31*(8), L08806. https://doi.org/10.1029/2003GL018166

Chisham, G., & Freeman, M. P. (2003). A technique for accurately determining the cusp-region polar cap boundary using superdarn hf radar measurements. *Annales Geophysicae*, *21*(4), 983–996. https://doi.org/10.5194/angeo-21-983-2003

Doe, R. A., Kelly, J. D., & Sánchez, E. R. (2001). Observations of persistent dayside f region electron temperature enhancements associated with soft magnetosheathlike precipitation. *Journal of Geophysical Research*, *106*(A3), 3615–3630. https://doi.org/10.1029/2000JA000186

Emmert, J. T., Drob, D. P., Picone, J. M., Siskind, D. E., Jones, M., Mlynczak, M. G., et al. (2021). Nrlmsis 2.0: A whole-atmosphere empirical model of temperature and neutral species densities. *Earth and Space Science*, *8*(3), e2020EA001321. https://doi.org/10.1029/2020EA001321

Fasel, G. J., Minow, J. I., Smith, R. W., Deehr, C. S., & Lee, L. C. (1992). Multiple brightenings of transient dayside auroral forms during oval expansions. *Geophysical Research Letters*, *19*(24), 2429–2432. https://doi.org/10.1029/92GL02103

Frey, H. U., Han, D., Kataoka, R., Lessard, M. R., Milan, S. E., Nishimura, Y., et al. (2019). Dayside aurora. *Space Science Reviews*, *215*(8), 51. https://doi.org/10.1007/s11214-019-0617-7

Friis-Christensen, E., Lühr, H., Knudsen, D., & Haagmans, R. (2008). Swarm – An earth observation mission investigating geospace. *Advances in Space Research*, *41*(1), 210–216. https://doi.org/10.1016/j.asr.2006.10.008

Gustavsson, B., Rietveld, M. T., Ivchenko, N. V., & Kosch, M. J. (2010). Rise and fall of electron temperatures: Ohmic heating of ionospheric electrons from underdense HF radio wave pumping. *Journal of Geophysical Research (Space Physics)*, *115*(A12), A12332. https://doi.org/10.1029/2010JA015873

Jin, Y., Moen, J. I., Spicher, A., Liu, J., Clausen, L. B. N., & Miloch, W. J. (2023). Ionospheric flow vortex induced by the sudden decrease in the solar wind dynamic pressure. *Journal of Geophysical Research: Space Physics*, *128*(11), e2023JA031690. https://doi.org/10.1029/2023JA031690

Johnsen, M. G., & Lorentzen, D. A. (2012a). The dayside open/closed field line boundary as seen from space- and ground-based instrumentation. *Journal of Geophysical Research (Space Physics)*, *117*(A3), A03320. https://doi.org/10.1029/2011JA016983

Johnsen, M. G., & Lorentzen, D. A. (2012b). A statistical analysis of the optical dayside open/closed field line boundary. *Journal of Geophysical Research (Space Physics)*, *117*(A2), A02218. https://doi.org/10.1029/2011JA016984

Johnsen, M. G., Lorentzen, D. A., Holmes, J. M., & Løvhaug, U. P. (2012). A model based method for obtaining the open/closed field line boundary from the cusp auroral 6300 Å[OI] red line. *Journal of Geophysical Research (Space Physics)*, *117*(A3), A03319. https://doi.org/10.1029/2011JA016980

King, J. H., & Papitashvili, N. E. (2005). Solar wind spatial scales in and comparisons of hourly wind and ace plasma and magnetic field data. *Journal of Geophysical Research*, *110*(A2), A02104. https://doi.org/10.1029/2004JA010649

Kofman, W., & Lilensten, J. (1992). Energy deposition in the E and F regions of the high-latitude ionosphere. *Advances in Space Research*, *12*(6), 137–146. https://doi.org/10.1016/0273-1177(92)90047-2

Kofman, W., & Wickwar, V. B. (1984). Very high electron temperatures in the daytime F region at Sondrestrom. *Geophysical Research Letters*, *11*(9), 919–922. https://doi.org/10.1029/GL011i009p00919

Kwagala, N. K., Oksavik, K., Lorentzen, D. A., & Johnsen, M. G. (2017). On the contribution of thermal excitation to the total 630.0 nm emissions in the northern cusp ionosphere. *Journal of Geophysical Research: Space Physics*, *122*(1), 1234–1245. https://doi.org/10.1002/2016JA023366

Lihtinen, M. S., & Huuskonen, A. (1996). General incoherent scatter analysis and GUISDAP. *Journal of Atmospheric and Solar-Terrestrial Physics*, *58*(1–4), 435–452. https://doi.org/10.1016/0021-9169(95)00047-x

Lockwood, M., Davies, J. A., Moen, J., van Eyken, A. P., Oksavik, K., McCrea, I. W., & Lester, M. (2005). Motion of the dayside polar cap boundary during substorm cycles: Ii. generation of poleward-moving events and polar cap patches by pulses in the magnetopause reconnection rate. *Annales Geophysicae*, *23*(11), 3513–3532. https://doi.org/10.5194/angeo-23-3513-2005

Lockwood, M., Moen, J., van Eyken, A. P., Davies, J. A., Oksavik, K., & McCrea, I. W. (2005a). Motion of the dayside polar cap boundary during substorm cycles: I. Observations of pulses in the magnetopause reconnection rate. *Annales Geophysicae*, *23*(11), 3495–3511. https://doi.org/10.5194/angeo-23-3495-2005

Lockwood, M., Moen, J., van Eyken, A. P., Davies, J. A., Oksavik, K., & McCrea, I. W. (2005b). Motion of the dayside polar cap boundary during substorm cycles: I. Observations of pulses in the magnetopause reconnection rate. *Annales Geophysicae*, *23*(11), 3495–3511. https://doi.org/10.5194/angeo-23-3495-2005

Löfås, H., Ivchenko, N., Gustavsson, B., Leyser, T. B., & Rietveld, M. T. (2009). F-region electron heating by X-mode radiowaves in underdense conditions. *Annales Geophysicae*, *27*(6), 2585–2592. https://doi.org/10.5194/angeo-27-2585-2009

Lorentzen, D. A., & Moen, J. (2000). Auroral proton and electron signatures in the dayside aurora. *Journal of Geophysical Research*, *105*(A6), 12733–12745. https://doi.org/10.1029/1999JA900405

Lorentzen, D. A., Moen, J., Oksavik, K., Sigernes, F., Saito, Y., & Johnsen, M. G. (2010). In situ measurement of a newly created polar cap patch. *Journal of Geophysical Research*, *115*(A12), A12323. https://doi.org/10.1029/2010JA015710

Lühr, H., Park, J., Gjerloev, J. W., Rauberg, J., Michaelis, I., Merayo, J. M. G., & Brauer, P. (2015). Field-aligned currents' scale analysis performed with the Swarm constellation. *Geophysics Research Letters*, *42*(1), 1–8. https://doi.org/10.1002/2014GL062453

McCrea, I., Aikio, A., Alfonsi, L., Belova, E., Buchert, S., Clilverd, M., et al. (2015). The science case for the EISCAT_3D radar. *Progress in Earth and Planetary Science*, *2*(1), 21. https://doi.org/10.1186/s40645-015-0051-8

McCrea, I. W., Lockwood, M., Moen, J., Pitout, F., Eglitis, P., Aylward, A. D., et al. (2000). ESR and EISCAT observations of the response of the cusp and cleft to IMF orientation changes. *Annales Geophysicae*, *18*(9), 1009–1026. https://doi.org/10.1007/s00585-000-1009-7

Mende, S. B., Frey, H. U., & Angelopoulos, V. (2016). Source of the dayside cusp aurora. *Journal of Geophysical Research: Space Physics*, *121*(8), 7728–7738. https://doi.org/10.1002/2016JA022657

Milan, S. E., Lester, M., Cowley, S. W. H., Moen, J., Sandholt, P. E., & Owen, C. J. (1999). Meridian-scanning photometer, coherent hf radar, and magnetometer observations of the cusp: A case study. *Annales Geophysicae*, *17*(2), 159–172. https://doi.org/10.1007/s00585-999-0159-5

Moen, J., Lockwood, M., Oksavik, K., Carlson, H. C., Denig, W. F., van Eyken, A. P., & McCrea, I. W. (2004). The dynamics and relationships of precipitation, temperature and convection boundaries in the dayside auroral ionosphere. *Annales Geophysicae*, *22*(6), 1973–1987. https://doi.org/10.5194/angeo-22-1973-2004

Newell, P. T., Meng, C.-I., Sibeck, D. G., & Lepping, R. (1989). Some low-altitude cusp dependencies on the interplanetary magnetic field. *Journal of Geophysical Research*, *94*(A7), 8921–8927. https://doi.org/10.1029/JA094iA07p08921

Newell, P. T., Ruohoniemi, J. M., & Meng, C. I. (2004). Maps of precipitation by source region, binned by IMF, with inertial convection streamlines. *Journal of Geophysical Research (Space Physics)*, *109*(A10), A10206. https://doi.org/10.1029/2004JA010499

Newell, P. T., Sotirelis, T., Liou, K., Meng, C. I., & Rich, F. J. (2006). Cusp latitude and the optimal solar wind coupling function. *Journal of Geophysical Research (Space Physics)*, *111*(A9), A09207. https://doi.org/10.1029/2006JA011731

Nilsson, H., Yamauchi, M., Eliasson, L., Norberg, O., & Clemmons, J. (1996). Ionospheric signature of the cusp as seen by incoherent scatter radar. *Journal of Geophysical Research (Space Physics)*, *101*(A5), 10947–10964. https://doi.org/10.1029/95JA03341

Nishimura, Y., Sadler, F. B., Varney, R. H., Gilles, R., Zhang, S. R., Coster, A. J., et al. (2021). Cusp dynamics and polar cap patch formation associated with a small IMF southward turning. *Journal of Geophysical Research (Space Physics)*, *126*(5), e29090. https://doi.org/10.1029/2020JA029090

Oksavik, K., Barth, V. L., Moen, J., & Lester, M. (2010). On the entry and transit of high-density plasma across the polar cap. *Journal of Geophysical Research*, *115*(A12), A12308. https://doi.org/10.1029/2010JA015817

Oksavik, K., Ruohoniemi, J. M., Greenwald, R. A., Baker, J. B. H., Moen, J., Carlson, H. C., et al. (2006). Observations of isolated polar cap patches by the European incoherent scatter (EISCAT) svalbard and super dual auroral radar network (SuperDARN) Finland radars. *Journal of Geophysical Research (Space Physics)*, *111*(A5), A05310. https://doi.org/10.1029/2005JA011400

Østgaard, N., Moen, J., Mende, S. B., Frey, H. U., Immel, T. J., Gallop, P., et al. (2005). Estimates of magnetotail reconnection rate based on image fuv and eiscat measurements. *Annales Geophysicae*, *23*(1), 123–134. https://doi.org/10.5194/angeo-23-123-2005

Schunk, R., & Nagy, A. (2009). *Ionospheres: Physics, plasma physics, and chemistry* (2). Cambridge University Press. (ISBN: 978-1-108-46210-5). https://doi.org/10.1017/CBO9780511635342

Schunk, R. W., Sojka, J. J., & Bowline, M. D. (1986). Theoretical study of the electron temperature in the high-latitude ionosphere for solar maximum and winter conditions. *Journal of Geophysical Research (Space Physics)*, *91*(A11), 12041–12054. https://doi.org/10.1029/JA091iA11p12041

Shepherd, S. G. (2014). Altitude-adjusted corrected geomagnetic coordinates: Definition and functional approximations. *Journal of Geophysical Research: Space Physics*, *119*(9), 7501–7521. https://doi.org/10.1002/2014JA020264

Shoucri, M. M., Morales, G. J., & Maggs, J. E. (1984). Ohmic heating of the polar F region by HF pulses. *Journal of Geophysical Research (Space Physics)*, *89*(A5), 2907–2917. https://doi.org/10.1029/JA089iA05p02907

Smith, A. R. A., Pačes, M., & Santillan, D. (2024). Esa-vires/vires-python-client. *Zenodo*. https://doi.org/10.5281/zenodo.10542661

Vennerstrom, S., Friis-Christensen, E., Jorgensen, T. S., Rasmussen, O., Clauer, C. R., & Wickwar, V. B. (1984). Ionospheric currents and F-region plasma boundaries near the dayside cusp. *Geophysical Research Letters*, *11*(9), 903–906. https://doi.org/10.1029/GL011i009p00903

Vontrat-Reberac, A., Fontaine, D., Blelly, P.-L., & Galand, M. (2001). Theoretical predictions of the effect of cusp and dayside precipitation on the polar ionosphere. *Journal of Geophysics Research*, *106*(A12), 28857–28866. https://doi.org/10.1029/2001JA900131

Watermann, J., Lummerzheim, D., de La Beaujardiere, O., Newell, P. T., & Rich, F. J. (1994). Ionospheric footprint of magnetosheathlike particle precipitation observed by an incoherent scatter radar. *Journal of Geophysical Research (Space Physics)*, *99*(A3), 3855–3868. https://doi.org/10.1029/93JA01995

Wickwar, V., & Kofman, W. (1984). Dayside red auroras at very high latitudes: The importance of thermal excitation. *Geophysical Research Letters*, *11*(9), 923–926. https://doi.org/10.1029/GL011i009p00923

Wild, J. A., Cowley, S. W. H., Davies, J. A., Khan, H., Lester, M., Milan, S. E., et al. (2001). First simultaneous observations of flux transfer events at the high-latitude magnetopause by the cluster spacecraft and pulsed radar signatures in the conjugate ionosphere by the cutlass and eiscat radars. *Annales Geophysicae*, *19*(10/12), 1491–1508. https://doi.org/10.5194/angeo-19-1491-2001

Xiong, C., Lühr, H., Wang, H., & Johnsen, M. G. (2014). Determining the boundaries of the auroral oval from CHAMP field-aligned current signatures - Part 1. *Annales Geophysicae*, *32*(6), 609–622. https://doi.org/10.5194/angeo-32-609-2014